



Modeling of the dynamic wetting behavior in a capillary tube considering the macroscopic–microscopic contact angle relation and generalized Navier boundary condition



Yasufumi Yamamoto^{a,*}, Katsunori Tokieda^b, Tatsuro Wakimoto^c, Takahiro Ito^d, Kenji Katoh^c

^a Department of Mechanical Engineering, Kansai University, 3-35, Yamate-cho 3-chome, Suita, Osaka 564-8680, Japan

^b Graduate School of Science and Engineering, Kansai University, 3-35, Yamate-cho 3-chome, Suita, Osaka 564-8680, Japan

^c Department of Mechanical Engineering, Osaka City University, 3-3-138, Sumiyoshi-ku Sugimoto, Osaka 558-8585, Japan

^d Department of Energy Engineering and Science, Nagoya University, Furo-cho Chikusa-ku, Nagoya 464-8603, Japan

ARTICLE INFO

Article history:

Received 21 August 2013

Received in revised form 28 October 2013

Accepted 31 October 2013

Available online 12 November 2013

Keywords:

Wetting

Moving contact line

Dynamic contact angle

Front-tracking method

Generalized Navier boundary condition

Microscopic–macroscopic dynamic angles' relation

ABSTRACT

In this study, dynamic wetting phenomena in a capillary tube were studied by using numerical simulations based on the front-tracking method employing the generalized Navier boundary condition (GNBC) and by experimental measurements. For the GNBC, based on molecular dynamics simulations, the microscopic dynamic contact angle is estimated from the grid-scale contact angle using Cox's macroscopic–microscopic relation. The experimentally measured correlation between the apparent dynamic contact angle and the moving velocity of the contact line is well reproduced by the present simulation technique considering Cox's macroscopic–microscopic relation. Thus, we found that the dynamics of wetting are well described by combining molecular-scale behavior and macroscopic–microscopic relations.

© 2013 Elsevier Ltd. All rights reserved.

1. Introduction

The wetting of a solid surface by a liquid is not only a physically interesting phenomenon but also critical in many industrial processes. When wetting or dewetting occurs, the contact line moves and the contact angle changes dynamically. The dynamics of the moving contact line is related to the dynamic contact angle, which has been studied by various researchers (e.g., see reviews by de Gennes, 1985; Bonn et al., 2009). In general, in continuum fluid dynamics, a solid surface is treated as a no-slip boundary. However, the contact line never moves (wetting or dewetting never occurs) and viscous stress diverges under the no-slip boundary condition. To reasonably represent the moving contact line, we have developed a new method on the basis of the generalized Navier boundary condition (GNBC) proposed by Qian et al. (2003) and combined it with the front-tracking method (Yamamoto et al., 2013). By using the grid-scale slip, the divergence of the viscous stress is avoided, and the experimentally observed dynamic properties can be well reproduced for very low capillary number conditions.

Yamamoto et al. (2013) considered the conditions for contact angles near 90° and small capillary numbers $O(10^{-3})$. In this paper, the conditions for very small contact angles and rather large capillary numbers are considered, and a dynamic wetting model is proposed and evaluated.

The GNBC model (Qian et al., 2003) is constructed on the basis of molecular dynamics (MD) simulation results. Based on a force-balance argument through careful MD studies, Qian et al. provided convincing evidence that the interfacial Young's stress still dominates the dynamic force balance in the region molecularly vicinity of the contact line. Therefore, the dynamic contact angle used in the GNBC is a microscopically (nm order) observed angle. However, we can obtain the grid-scale (μm – mm order) macroscopic contact angle in the front-tracking simulation with practical resolution. In some conditions (e.g., very low capillary number) reported by Yamamoto et al. (2013), the microscopic and macroscopic contact angles do not differ much; however, in general, they differ according to the analysis by Cox (1986). Thus, we introduce a new method that combines Cox's macroscopic–microscopic angle relation and the GNBC. In this method, the microscopic dynamic contact angle is estimated from Cox's relation and used in the GNBC for computing the moving contact line. To date, similar modeling efforts have been proposed for representing

* Corresponding author. Tel.: +81 6 6368 0375; fax: +81 6388 8785.

E-mail address: yamayas@kansai-u.ac.jp (Y. Yamamoto).

the unresolved microscopic behavior. For example, Afkhami et al. (2009) used an approximation of Cox's relation, Dupont and Legendre (2010) used a similar relation by Ngan and Dussan (1989), Sui and Spelt (2013) used Cox's relation with higher order. However, all of them consider a fixed static contact angle as a microscopic contact angle. Sui and Spelt (2013) compared their simulations with experimental data and showed that considering the microscopic contact angle as static leads to unrealistic microscopic length scales. In the proposed method, the unresolved microscopic behavior is treated in macroscopic scale simulations using Cox's relation. However, we considered a dynamic microscopic angle and applied the GNBC model to a microscopic dynamic contact angle and slip velocity relation. Unlike the hybrid method that combines molecular dynamics simulation and finite elements by (Hadjiconstantinou, 1999a,b), we use the GNBC just as a slip boundary condition. In addition, we compared the simulation results with experimental data and discuss the model parameters.

2. Numerical method

2.1. Front-tracking method

In the front-tracking method (Unverdi and Tryggvason, 1992), the gas–liquid interface is tracked by marker points and the interface information is calculated by elements connecting markers. Using this information, the single-fluid equations are solved by using the finite-difference method. In this study, the calculation was performed on the staggered grid system and axisymmetric cylindrical coordinate system, where x is the radial (horizontal) and y is the axial (vertical) direction. The velocity components are represented by u and v in the x - and y -direction, respectively.

2.2. Generalized Navier boundary condition (GNBC)

The GNBC was proposed by Qian et al. (2003) on the basis of MD simulations. One piece of evidence is that the tangential interaction force between the fluid molecules in a very thin layer adjacent to a wall and the wall molecules is proportional to the slip velocity. Another piece of evidence is that the interaction force acting on the very thin layer adjacent to the wall can be represented by the viscous shear stress on the wall $\tau_{\text{wall}}^{\text{visc}}$ and unbalanced Young's stress $\tilde{\tau}^{\text{Young}}$. The GNBC can then be represented as

$$\beta v_{\text{slip}} = \tau_{\text{wall}}^{\text{visc}} + \tilde{\tau}^{\text{Young}}, \quad (1)$$

where v_{slip} is the slip velocity on the wall and β is the slip coefficient. Unbalanced Young's stress is given by the integral,

$$\int_{\text{int}} \tilde{\tau}^{\text{Young}} dy = \sigma(\cos \theta_s - \cos \theta_d), \quad (2)$$

where θ_s and θ_d are the static and dynamic contact angle, respectively, σ is the surface tension of the liquid, and the integration is applied across the diffused interface along the direction parallel to the wall. Yamamoto et al. (2013) proposed a numerical implementation of the stress by an approximation of the delta function used in the front-tracking method,

$$\tilde{\tau}^{\text{Young}}(y_j) = \sigma(\cos \theta_s - \cos \theta_d) d(y_j - y_{\text{cl}}), \quad (3)$$

where y_j and y_{cl} are the positions of the j th grid point and the contact line, respectively. The approximated delta function d proposed by Peskin (2002) is given by,

$$d(r) = \begin{cases} \frac{1}{4\Delta} \left(1 + \cos \frac{\pi r}{2\Delta}\right), & |r| \leq 2\Delta, \\ 0, & |r| > 2\Delta, \end{cases} \quad (4)$$

where Δ is the grid spacing. θ_d is calculated by the three-marker-point Lagrangean approximation. Then, v_{slip} is obtained from Eq.

(1) with Eqs. (3) and (4), and used as the boundary conditions on the wall.

2.3. Simplification of GNBC

Using the GNBC, the divergence of the viscous stress is avoided because the large slip velocity occurs at the contact line. Moreover, owing to the decrease in the viscous stress, the first term of the right-hand side of Eq. (1) is negligible compared with the second term. Thus, only the slip velocity due to unbalanced Young's stress near the contact line is accounted in Eq. (1). In the region far from the contact line, the no-slip condition is applied. We refer to this boundary condition as the simplified GNBC (SGNBC). In the conditions considered in this study, there is no significant difference between the SGNBC and GNBC in the simulations. The same type of slip models was also considered by Ren and E (2007).

By using the SGNBC, the nondimensional contact line velocity (i.e., capillary number $Ca \equiv \mu v_{\text{cl}}/\sigma$, where μ is the viscosity of the liquid phase and v_{cl} is the contact line velocity corresponding to $v_{\text{slip}}(y_{\text{cl}})$) is derived by Eqs. (1), (3), and (4) with $y = y_{\text{cl}}$ and neglecting $\tau_{\text{wall}}^{\text{visc}}$,

$$Ca = \chi(\cos \theta_s - \cos \theta_d), \quad (5)$$

where $\chi(= \bar{\mu}/(\beta\Delta))$ is the nondimensional slip parameter that represents the dynamic property of wetting. $\bar{\mu}$ is the arithmetic average viscosity, and this treatment is discussed in the electronic Annex 1 in the online version of the Yamamoto et al. (2013) study. Because we use resolution-dependent distributions of the interfacial information in the front-tracking procedure, Eq. (3) also depends on the grid resolution Δ . Thus, slip coefficient β is no longer a physical parameter, and parameter χ should be treated as the nondimensional slip parameter as confirmed by Yamamoto et al. (2013). It is found from Fig. 9(a) and (b) in Yamamoto et al. (2013) that Young's stress is much larger (100 times or more) than viscous stress at the contact line with any resolution. And it is found from Fig. 13 in Yamamoto et al. (2013) that the capillary number is perfectly proportional to cosine of the dynamic contact angle in the same manner as Eq. (5). So we consider that the viscous term in the GNBC can be neglected.

Eq. (5) represents the slip related to the deviation of the instantaneous contact angle from the static contact angle, and the contact line moves making the contact angle to approach the static contact angle. The parameter χ characterizes the response time of the contact line movement. A large χ results in large Ca and then the contact angle rapidly approaches the static angle. Then, the wall slip velocity is given in the form using Ca from Eqs. (1), (3), (5) and delta function distribution $2\Delta d$ as

$$v_{\text{slip}}(y_j) = Ca \frac{\sigma}{\mu} 2\Delta d(y_j - y_{\text{cl}}). \quad (6)$$

2.4. Estimation of the microscopic contact angle using Cox's relation

Because the GNBC is constructed on the basis of MD simulations, the dynamic contact angle in Eq. (5) should be microscopically measured as

$$Ca = \chi(\cos \theta_s - \cos \theta_d^{\text{micro}}). \quad (7)$$

However, in the front-tracking method, the obtained contact angles are macroscopically measured in the grid scale (marker intervals are between 0.6Δ and 0.8Δ). Therefore, we used the relation between the macroscopic contact angle θ_d^{macro} and the microscopic angle θ_d^{micro} derived by Cox using the matched asymptotic expansion (Cox, 1986)

$$G(\theta_d^{\text{macro}}) = G(\theta_d^{\text{micro}}) + Ca \ln \left(\frac{l^{\text{macro}}}{l^{\text{micro}}} \right) + O(Ca), \quad (8)$$

where l^{macro} and l^{micro} are the macroscopic and microscopic characteristic length scales, respectively.

Similar relations were also derived by Ngan and Dussan (1989) and Hocking and Rivers (1982). In these analyses, the flow field is divided into microscopic, macroscopic and intermediate scales. In the macroscopic (outer) and intermediate regions, the no-slip boundary condition is considered. In the microscopic (inner) region, the slip boundary condition is allowed; however, the no-slip condition is considered at the outer limit of the inner region. In all scales, the flow field is expanded as perturbations of the Ca and Stokes equations for the zeroth-order field are solved. The normal stress conditions obtained from the zeroth-order field are connected to the capillary effect of interface deformation. By matching the inner and outer regions via the intermediate region, the macroscopic dynamic contact angle is related to the microscopic angle on the wall. Cox (1986) did not consider the full microscopic behavior, only the outer limit of the inner region. Cox supposed the microscopic contact angle is static; however, we consider the microscopic angle can be dynamic.

Function G is complex and lengthy, but it is well approximated in the case of the zero viscosity ratio and $\theta < (3/4)\pi$ as $G(\theta) = (1/9)\theta^3$ (Kistler, 1993; Blake, 2006). Then, Eq. (8) is given in the simple form

$$(\theta_d^{\text{macro}})^3 = (\theta_d^{\text{micro}})^3 + 9Ca \ln \left(\frac{l^{\text{macro}}}{l^{\text{micro}}} \right). \quad (9)$$

According to this relation, θ_d^{micro} can be estimated from grid-scale angle θ_d^{grid} as θ_d^{macro} with $l^{\text{macro}} = \Delta$,

$$(\theta_d^{\text{micro}})^3 = (\theta_d^{\text{grid}})^3 - 9Ca \ln \left(\frac{\Delta}{l^{\text{micro}}} \right). \quad (10)$$

Then, θ_d^{micro} can be used in Eq. (7) for the SGNBC. When calculating Eq. (10), Ca is not obtained. Therefore, Eqs. (7) and (10) were simultaneously solved by using Newton's iteration method. Though the new parameter l^{micro} should be predetermined, the determination from experimental data is discussed later. We consider that the microscopic contact angle is not static but dynamic, as described in the GNBC. This concept greatly differs from the studies reported by Afkhami et al. (2009), Dupont and Legendre (2010), and Sui and Spelt (2013).

The SGNBC-Front-tracking procedure with Cox's relation is summarized as follows. The velocities of the front markers are interpolated from the grid points, and the positions of the markers are updated. The densities and viscosities on the grid points are updated for the new interface positions. The interfacial tension force and the grid-scale dynamic contact angle θ_d^{grid} are calculated by the marker positions. The microscopic dynamic contact angle θ_d^{micro} and the nondimensional contact line velocity Ca are calculated with Eqs. (7) and (10). The velocity on the wall v_{slip} is calculated with Eq. (6). The Navier–Stokes and continuity equations are solved with the boundary condition v_{slip} and then the flow field is updated.

2.5. Resolution dependency test

Afkhami et al. (2009) used the volume of fluid method to show the resolution dependency of the contact line problems. Similarly, in this study, simple tests were performed to examine the resolution dependency of the contact line model. The configuration of the test of the flat plate immersion is shown in Fig. 1. The domain size is set to $2l_{\text{cap}}$ in the horizontal and $4l_{\text{cap}}$ in the vertical direction, where the capillary length is $l_{\text{cap}} = [\sigma/(\rho g)]^{1/2}$ and ρ and g are the liquid density and gravitational acceleration, respectively. The lower 2/3 portion was filled with 86% water–glycerol and upper 1/3 with air. The static contact angle was 65° and χ was

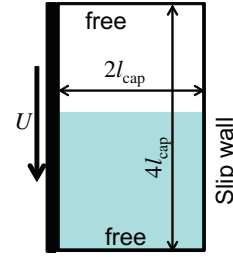


Fig. 1. Configuration of the resolution dependency test.

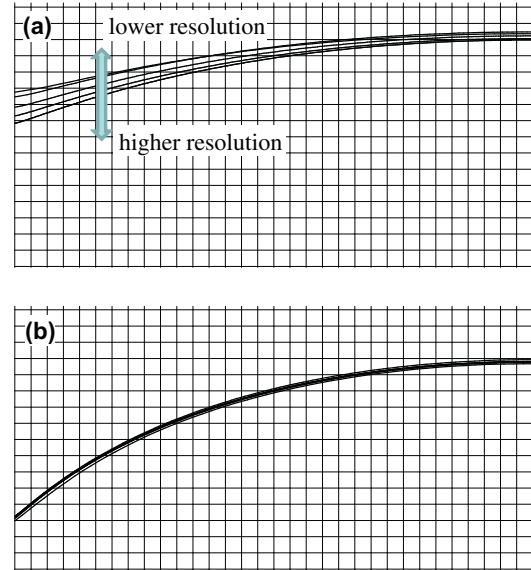


Fig. 2. Steady-state interfaces at different grid resolutions, $l_{\text{cap}}/\Delta = 16, 32, 64, 128, 256$. (a) For that θ_d^{grid} as θ_d in Eq. (5) without Cox's relation and (b) for θ_d^{micro} as θ_d with Cox's relation and $l^{\text{micro}} = 10^{-9}$ m. The grid shown is the lowest one.

0.1. The velocity of the wall was set as the capillary number corresponding to 0.055 as in the experiments by Blake and Shikhmurzaev (2002). Gravity was controlled to act only in the region where the phase is replaced from the initial condition. The computations in this section were performed in two-dimensional coordinates and not axisymmetrically.

Figs. 2 and 3 show the steady-state interface shape and time evolution of the contact line positions. When θ_d^{grid} is used as θ_d (Eq. (5)), without Cox's relation, the results depend on the grid resolutions (Figs. 2(a) and 3(a)). From Fig. 3(a), the variation of the resolution in geometrical progression causes the variation of the contact line positions in arithmetical progression, namely, there is logarithmic dependency, and grid convergence cannot be obtained. On the other hand, in the case that θ_d^{micro} estimated from Cox's relation (10) with $l^{\text{micro}} = 10^{-9}$ m is used in Eq. (7), the results are almost independent of the grid resolution as shown in Figs. 2(b) and 3(b). As shown in Fig. 4, the resolution dependency of the results without Cox's relation is logarithmic. The results with Cox's relation and $l^{\text{micro}} = 10^{-9}$ m correspond to the meniscus height supposedly computed without Cox's relation and $\Delta = 10^{-9}$ m. Therefore, by using Cox's relation, we can simulate the flow field containing the effect of the microscopic scale behavior without microscopic scale resolution.

3. Capillary tube experiment

As the simulation target in this study, we chose the problem of a liquid column rise in a capillary tube because it is a simple system

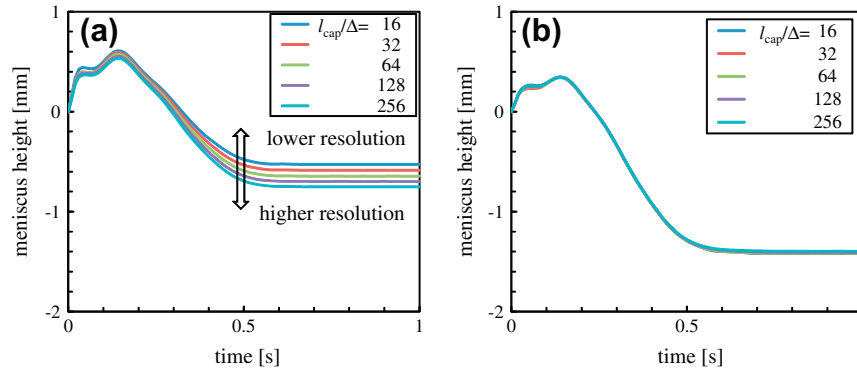


Fig. 3. Dependence of the time-varying contact line position on grid spacing. (a) Case for θ_d^{grid} as θ_d in Eq. (5) without Cox's relation and (b) for θ_d^{micro} as θ_d with Cox's relation and $l^{\text{micro}} = 10^{-9}$ m.

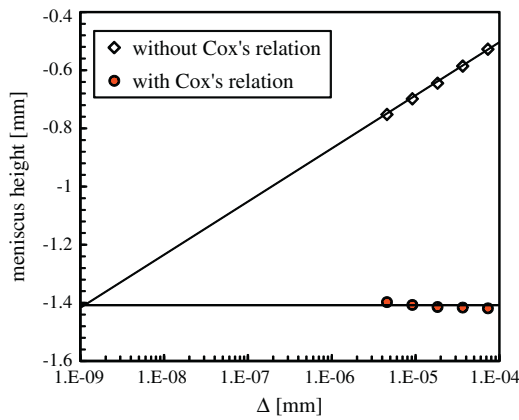


Fig. 4. Dependence of the steady-state contact line positions on grid spacing. In the case of Cox's relation, l^{micro} is 10^{-9} m.

and unsteadiness is observed easily. We compared the results of the simulations with experimental data and then discussed the temporal development of the rising liquid, the correlation between velocity and angle, and the model parameters. The overview of the experimental setup and method is described in more detail in Kato et al. (2010). The combination of test fluids and capillary tubes is shown in Table 1. The tubes are submerged to 5 mm depth in the fluid pool. The liquid surface in the tube was photographed by using a CCD camera. The height of the liquid column center and the contact line position were measured from PC-captured images at a rate of 250 (Hz). The profile of the whole interface in the tube diameter d_p was calculated by solving the axisymmetric Laplace equation

$$\sigma \left\{ -\frac{d^2b/dx^2}{[1 + (db/dx)^2]^{3/2}} - \frac{db/dx}{x[1 + (db/dx)^2]^{1/2}} \right\} = -\rho g b + \delta p, \quad (11)$$

Table 1
Liquid–solid combination condition.

Case	A	B
Liquid	Ethylene glycol	Glycerin 50% water
Density, ρ (kg/m ³)	1115	1125
Viscosity, μ (Pa s)	0.02	0.006
Surface tension, σ (mN/m)	48.6	67.9
Tube	Glass	Glass
Diameter, d_p (mm)	1.024	1.024
Static contact angle, θ_s (°)	15.3	37.08

where b is the height from the meniscus at the radial position x and δp is the pressure jump at the trough. The boundary conditions at the tube center and wall are $db/dx = 0$ and $b = 0$ at $x = 0$, and $b = b_{\text{wall}}$ at $x = d_p/2$, where b_{wall} indicates the meniscus height at the wall as measured from the digital images with an accuracy of about 1 pixel (4 μ m). The numerical solution of Eq. (11) satisfying the above boundary conditions was obtained by repeatedly correcting δp as per Newton's method. The contact angle was calculated from the tangent of the meniscus curve at the wall. The scatter of the measurements of the contact angle was within $\pm 1^\circ$, that of the liquid column height was within ± 0.03 mm, and the reproducibility was checked carefully. The dynamic contact angle was measured from the calculated profile for a tube with diameter. Therefore, the measured scale of the contact angle is characterized by the tube diameter, $l^{\text{macro}} \sim d_p$.

4. Results and discussion

The boundary conditions for the capillary tube simulation are shown in Fig. 5. The properties of the liquid and the tube are shown in Table 1. The gas phase is assumed to have the density and viscosity of air, $\rho_g = 1.205$ kg/m³ and $\mu_g = 1.822 \times 10^{-5}$ Pa s, respectively. The initial liquid height H_b , corresponding to the surface height of the reserved liquid outside the tube, was set at 5×10^{-3} m to coincide with the experimental conditions. We used the grid resolutions and the time increments in Table 2.

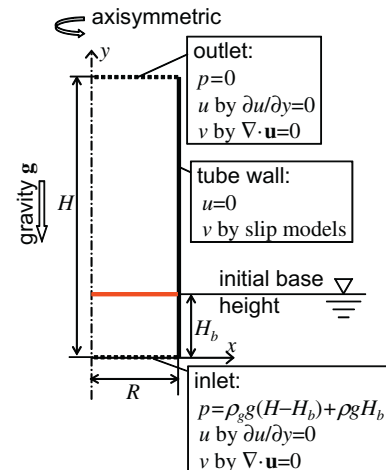


Fig. 5. Boundary conditions for the capillary tube simulations.

Table 2

Grid resolution and time increment condition. A and B represent the liquid–solid conditions in Table 1.

Case	A low	A high	B low	B high
Number of grid points	16 × 768	32 × 1536	16 × 832	32 × 1664
Grid spacing (μm)	64	32	64	32
Time increment (μs)	2.5	1.25	2	1

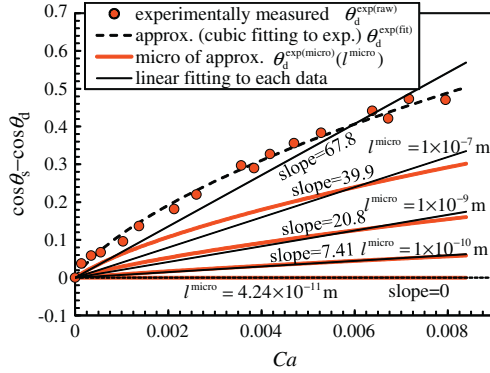


Fig. 6. Relation between Ca and $\cos \theta_d$ for the experimentally measured data and estimated microscopic angles (ethylene glycol–glass case).

Fig. 6 shows the relation between the nondimensional contact line velocity Ca and the difference in the cosines of the contact angles for ethylene glycol in the glass tube experiment. The bold broken line in Fig. 6 shows the cubic fit to data $\theta_d^{\text{exp(fit)}}$ of the experimentally measured angle $\theta_d^{\text{exp(raw)}}$ (circles). The bold solid lines (red in the online version) show the estimated microscopic dynamic contact angles $\theta_d^{\text{exp(micro)}}$ at some l^{micro} by using Eq. (10) with the fitted data $\theta_d^{\text{exp(fit)}}$ as θ_d^{macro} and the tube diameter d_p as l^{macro} .

$$\theta_d^{\text{exp(micro)}}(l^{\text{micro}}) = \left[(\theta_d^{\text{exp(fit)}})^3 - 9Ca \ln \left(\frac{d_p}{l^{\text{micro}}} \right) \right]^{1/3}. \quad (12)$$

The thin solid lines show the linear fit for each $\theta_d^{\text{exp(micro)}}(l^{\text{micro}})$. If raw experimental measured data, which have some scatters, are converted by Eq. (12), the scatters are magnified and the characteristics of the velocity angle relation are difficult to see. So we applied fitting at first, then microscopic contact angles are estimated from the fitting data.

The cosine of the apparent (macroscopic) contact angles $\theta_d^{\text{exp(raw)}}$ (or $\theta_d^{\text{exp(fit)}}$) does not show linear relation with Ca unlike Eq. (5). This curved profile of the macroscopic contact angle shows that the macroscopic contact angle is not decided only by the Young's stress. Thus we employ the Cox's macroscopic–microscopic relation with the GNBC. On the other hand, the cosine of the estimated microscopic contact angles $\theta_d^{\text{exp(micro)}}$ with small l^{micro} shows almost linear relation with Ca . In such cases, the reciprocal of the slope should correspond to nondimensional slip parameter χ in Eq. (7). Thus, by finding l^{micro} , at which the cosine of the estimated microscopic contact angle shows linear relation with Ca using experimental data, the nondimensional slip parameter χ is determined automatically. For example, in this case, $l^{\text{micro}} = 10^{-9}$ m almost gives a linear relation and χ is $1/20.8 = 0.048$.

Fig. 7 shows the relation between the contact line velocity and the dynamic contact angle for ethylene glycol in the glass tube simulations. N is the number of grid points per tube radius. The results without Cox's relation (broken line) cannot reproduce the curved profile of the experimental data. In this case, χ is determined from the slope of the forcibly linear fit as $1/67.8 = 0.015$

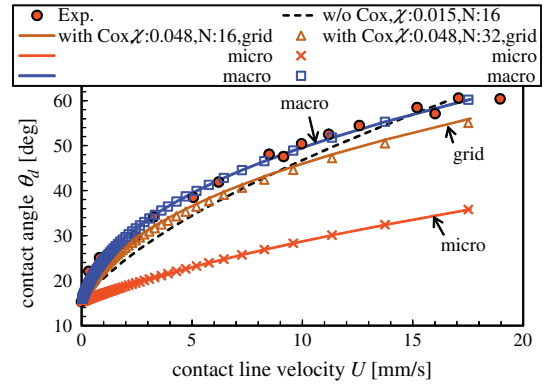


Fig. 7. Relation between contact line velocity and dynamic contact angle (ethylene glycol–glass case). N denotes the number of grid points per tube radius.

in Fig. 6. For the results with Cox's relation, three types of dynamic contact angles are shown: the grid-scale contact angle θ_d^{grid} at Δ , the microscopic θ_d^{micro} at l^{micro} , and the pipe-diameter-scale macroscopic θ_d^{macro} at d_p . The microscopic contact angle θ_d^{micro} was estimated from θ_d^{grid} using Eq. (10) with $l^{\text{micro}} = 10^{-9}$ m. The macroscopic dynamic angle θ_d^{macro} was calculated from θ_d^{micro} using Eq. (9) with $l^{\text{macro}} = d$. The grid-scale contact angles θ_d^{grid} for two resolutions ($N = 16$ and 32) are smaller than the experimentally measured angles and slightly dependent on the grid-resolution. The microscopic contact angles θ_d^{micro} are smaller than the grid-scale and the experimental contact angles, and are independent of the resolution. The macroscopic dynamic angles at pipe diameter scale θ_d^{macro} are in very good agreement with the experimentally measured angles. Therefore, the GNBC with Cox's relation can well reproduce the experimentally observed correlation, and attention should be paid to the observation scale for the comparison between the macroscopic dynamic contact angles.

Fig. 8 shows the liquid column heights as a function of time for ethylene glycol in the glass tube simulations. The theoretical solution of the Washburn equation (Lucas, 1918; Washburn, 1921; Bosanquet, 1923) with a fixed static contact angle shows extremely fast rising, which confirmed that considering the dynamic contact angle is very important. The results with Cox's relation ($\chi = 0.048$, $l^{\text{micro}} = 10^{-9}$ m, $N = 16$ and 32) agree with the experimental data. The results with χ determined from Fig. 6 can reproduce the experimentally observed behavior very well regardless of the resolution.

Though the result without Cox's relation ($\chi = 0.015$) also agrees with the experimental data in Fig. 8, the differences, shown in Fig. 7, may cause the deviations in the case of the more complex

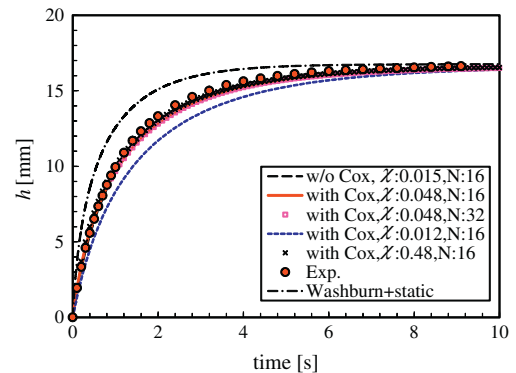


Fig. 8. Liquid column heights as a function of time (ethylene glycol–glass case). N represents the number of grid points per tube radius.

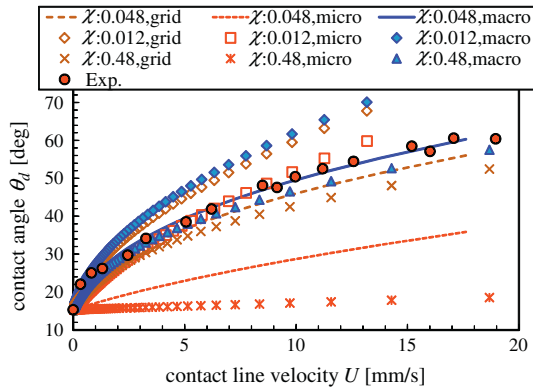


Fig. 9. Effect of the nondimensional slip parameter on the relation between the contact line velocity and dynamic contact angle (ethylene glycol–glass case), $l^{\text{micro}} = 10^{-9}$ m.

flow configuration. The results for modified χ 1/4 times as small and 10 times as large as $\chi = 0.048$ determined from Fig. 6, are also shown in Fig. 8. The small χ value slows the upward speed, and the behavior does not agree with the experiment; however, large χ cases seem to converge to similar results. Computation without Cox's relation with large χ (as shown in Yamamoto et al. (2013)) results in fast rising speeds similar to the theoretical results with a fixed static angle in Fig. 8. However, computations with Cox's relation and large χ give convergent results because large χ values make the microscopic dynamic contact angle to rapidly approach the static one in accordance with Eq. (7). Fig. 9 shows the effect of the nondimensional parameter χ on the relation of the contact line velocity and the dynamic contact angle. It is found that the maximum velocity (represented by the most right plot) for small χ (0.012) is smaller than the others. Because the contact line velocity is determined by Eq. (7), the small χ value cannot reproduce the fast movement as represented by the experimental data. The large χ can reproduce the fast movement, however, the microscopic contact angle rapidly approaches the static angle, and then the contact line velocity never increases. Hence, using Cox's relation combined with the GNBC and large χ corresponds to the case that the microscopic dynamic contact angle being the static contact angle. In the case of ethylene glycol in the glass tube in this study, the apparent contact angle estimated with $\theta_d^{\text{micro}} = \theta_s$ and $l^{\text{micro}} = 10^{-9}$ m is accidentally close to the experimental data; consequently, the column rising behavior converges close to the experimental data.

Fig. 10 shows the results of glycerin with 50% water. The experimental data show the curved profile. The linear fit does not represent such curved profile. The curved profile is reproduced by the macroscopic angle obtained from Cox's relation. In this case, the present simulation with the adjusted parameters ($l^{\text{micro}} = 10^{-9}$ m and $\chi = 0.017$), determined by using the same procedure as above, can also very well reproduce the experimental data (time history of liquid height and the velocity–angle correlation). Thus, we consider that the microscopic wetting behavior is well described by the GNBC, and the macroscopic wetting behavior well correlates with the microscopic using Cox's relation.

As shown in Figs. 6 and 10(a), adjusting l^{micro} , the zero slope (i.e., the microscopic angle corresponds to the static angle regardless of Ca) may be obtained. However, in such cases, l^{micro} takes unrealistically small values (e.g., $l^{\text{micro}} \sim 10^{-11}$ m for ethylene glycol; $l^{\text{micro}} \sim 10^{-17}$ m for glycerin as shown in each figure), indicating that the microscopic angle is not a static contact angle. At the microscopic scale l^{micro} , microscopic dynamics (such as described by the GNBC) decides the microscopic dynamic angle via the interaction with macroscopic behavior as described by Cox's relation.

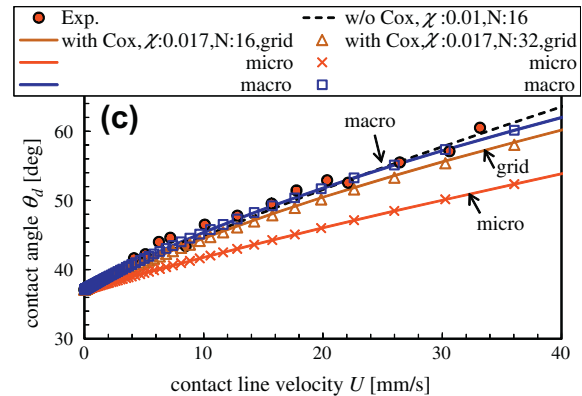
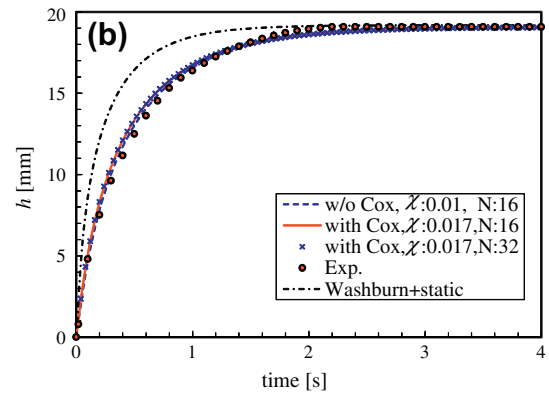
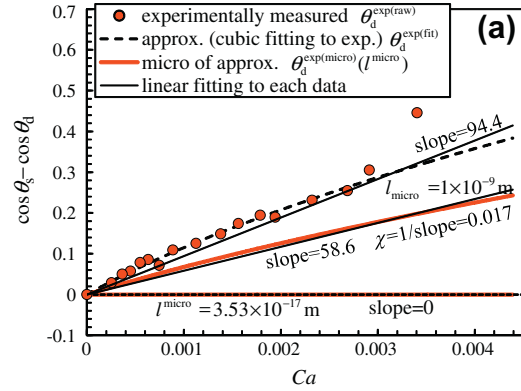


Fig. 10. Results for glycerin and 50% water. N is the number of grid points per tube radius. (a) Relation between Ca and $\cos \theta_d$ for the experimentally measured data and estimated microscopic angles. (b) Liquid column height as a function of time. (c) Relation between contact line velocity and dynamic contact angle. For (b) and (c), l^{micro} is 10^{-9} m and is determined from the relation in (a).

The adjusted parameter l^{micro} is in log function of Eq. (12), so not strict value but the scale order is important. A little change of l^{micro} does not affect the simulation results observed macroscopically.

5. Conclusion

A numerical wetting model was proposed on the basis of the front-tracking method, the GNBC, and the Cox's macroscopic–microscopic relation. The grid-resolution independency of the proposed wetting model using Cox's relation was confirmed. We also demonstrated how to determine the model parameters of microscopic length scale l^{micro} and nondimensional slip parameter χ by analyzing the experimental data for capillary tube flow. As l^{micro} is adjusted to represent the linear relation between the

microscopic dynamic contact angle and the moving velocity of the contact line from experimentally measured data, χ is automatically determined by the slope of the fit. Thus, we found that the dynamics of wetting is well described by combination of molecular scale behavior (GNBC) and macroscopic–microscopic relation (Cox's) very well. Tests for different conditions and inertial rapid wetting cases, such as in Sui and Spelt (2013) and Cox (1998), will be examined in the future.

Acknowledgment

This study was partially supported by JSPS KAKENHI Grant No. 25420135.

References

- Afkhami, S., Zaleski, S., Bussmann, M., 2009. A mesh-dependent model for applying dynamic contact angles to VOF simulations. *J. Comput. Phys.* 228, 5370–5389.
- Blake, T.D., 2006. The physics of moving wetting lines. *J. Colloid Interface Sci.* 299, 1–13.
- Blake, T.D., Shikhmurzaev, Y.D., 2002. Dynamic wetting by liquids of different viscosity. *J. Colloid Interface Sci.* 253, 196–202.
- Bonn, D., Eggers, J., Indekeu, J., Meunier, J., Rolley, E., 2009. Wetting and spreading. *Rev. Mod. Phys.* 81, 739–805.
- Bosanquet, C.H., 1923. On the flow of liquids into capillary tubes. *Philos. Mag. Ser. 6*, 525–531.
- Cox, R., 1986. The dynamics of the spreading of liquids on a solid surface. Part 1. Viscous flow. *J. Fluid Mech.* 168, 169–194.
- Cox, R., 1998. Inertial and viscous effects on dynamic contact angles. *J. Fluid Mech.* 357, 249–278.
- de Gennes, P.G., 1985. Wetting: statics and dynamics. *Rev. Mod. Phys.* 57, 827–863.
- Dupont, J.-B., Legendre, D., 2010. Numerical simulation of static and sliding drop with contact angle hysteresis. *J. Comput. Phys.* 229, 2453–2478.
- Hadjiconstantinou, N.G., 1999a. Combining atomistic and continuum simulations of contact-line motion. *Phys. Rev. E* 59, 2475–2478.
- Hadjiconstantinou, N.G., 1999b. Hybrid atomistic–continuum formulations and the moving contact-line problem. *J. Comput. Phys.* 154, 245–265.
- Hocking, L.M., Rivers, A.D., 1982. The spreading of a drop by capillary action. *J. Fluid Mech.* 121, 425–442.
- Katoh, K., Wakimoto, T., Nitta, S., 2010. A study on capillary flow under the effect of dynamic wetting. *J. Jpn. Soc. Exp. Mech.* 10, s62–s66.
- Kistler, S.F., 1993. Hydrodynamics of wetting. In: Berg, J.C. (Ed.), *Wettability*. Marcel Dekker, pp. 311–429.
- Lucas, R., 1918. Ueber das Zeitgesetz des kapillaren aufstiegs von flüssigkeiten. *Kolloid Z.* 23, 15–22.
- Ngan, C.G., Dussan, V.E.B., 1989. On the dynamics of liquid spreading on solid surfaces. *J. Fluid Mech.* 209, 191–226.
- Peskin, C.S., 2002. The immersed boundary method. *Acta Numer.* 11, 479–517.
- Qian, T., Wang, X.P., Sheng, P., 2003. Molecular scale contact line hydrodynamics of immiscible flows. *Phys. Rev. E* 68, 016306–1–016306–15.
- Ren, W., E, W., 2007. Boundary conditions for the moving contact line problem. *Phys. Fluids* 19, 022101–1–15.
- Sui, Y., Spelt, P.D.M., 2013. An efficient computational model for macroscale simulations of moving contact lines. *J. Comput. Phys.* 242, 37–52.
- Unverdi, S.O., Tryggvason, G., 1992. A front-tracking method for viscous, incompressible, multi-fluid flows. *J. Comput. Phys.* 100, 25–37.
- Washburn, E.W., 1921. The dynamics of capillary flow. *Phys. Rev.* 17, 273–283.
- Yamamoto, Y., Ito, T., Wakimoto, T., Katoh, K., 2013. Numerical simulations of spontaneous capillary rises with very low capillary numbers using a front-tracking method combined with generalized Navier boundary condition. *Int. J. Multiphase Flow* 51, 22–32.